Soft Matter

Temperature-controlled dripping-onto-substrate (DoS) extensional rheometry of polymer micelle solutions

Journal:	*Soft Matter*
Manuscript ID	SM-ART-03-2022-000377.R1
Article Type:	Paper
Date Submitted by the Author:	20-Apr-2022
Complete List of Authors:	Zhang, Diana; University of Minnesota Twin Cities, Chemical Engineering and Materials Science Calabrese, Michelle; University of Minnesota System, Chemical Engineering and Materials Science;

Soft Matter

ARTICLE TYPE

Cite this: DOI: 00.0000/xxxxxxxxxx

Temperature-controlled dripping-onto-substrate (DoS) extensional rheometry of polymer micelle solutions†

Diana Y. Zhang[a] and Michelle A. Calabrese*[a]

Received Date
Accepted Date

DOI: 00.0000/xxxxxxxxxx

Capillary-driven thinning of a liquid bridge is commonly used to measure the extensional rheology of macromolecular solutions for assessment of material sprayability, printability, and jettability. Methods like dripping-onto-substrate (DoS) rheometry are often preferred to methods like capillary breakup extensional rheometry (CaBER) due to low required sample volume and ability to measure low-viscosity fluids; however, DoS measurements to-date have been limited to ambient temperatures. Here, an environmental control chamber is developed to enable temperature-controlled DoS (TC-DoS) measurements, and the temperature-dependent extensional rheology of a model system poloxamer 234 (P234) in NaF brine is examined. Spherical P234 micelles at ambient conditions exhibit inertiocapillary (IC) thinning; above the sphere-to-rod transition temperature, the liquid bridge evolves towards viscocapillary (VC) thinning as micelles elongate and shear viscosity increases. Above 37 °C, wormlike micelle (WLM) formation results in pronounced elastocapillary (EC) thinning, and further WLM growth and entanglement results in three elasticity-dominated flow regimes: EC thinning, beads-on-a-string (BOAS) instability formation, and BOAS thinning. Despite having a substantially larger amphiphile molecular weight and micelle cross-sectional radius than surfactant WLMs, entangled P234 WLMs exhibit similar extensional behavior and achieve comparable maximum Trouton ratios. Comparing DoS measurements on P234 WLMs with prior studies on surfactant WLMs reveals that the maximum Trouton ratio depends on the ratio of shear and extensional relaxation times, a trend undetectable via CaBER due to pre-deformation during the initial step stretch. These findings reveal rich temperature-dependent flow behaviors in polymer micelles and highlight the importance of using a minimally-disruptive method such as TC-DoS when measuring the extensional rheology of microstructured and thermosensitive fluids.

1 Introduction

Industrially-relevant processes such as spraying and atomization,[1,2] printing,[3,4] jetting,[5] and roll-to-roll coating[6–8] are dominated by strong extensional flows in which fluids undergo capillary-driven thinning and breakup. Temperature is an important environmental factor that can impact fluid behavior during processing. For example, temperature differences between the spraying liquid and surrounding air can affect droplet size[1]; Hoffmann *et al.*[9] showed that these differences resulted from temperature-dependent changes in fluid properties such as surface tension and viscosity. Temperature-dependent properties can thus be exploited to make materials more processable via methods such as spraying and printing. As such, understanding the impact of temperature and fluid properties on the nature of capillary-driven thinning and breakup is essential for determining their processability. Extensional rheology measurements enable the determination of properties such as extensional relaxation time, extensional viscosity, and drop breakup time – all of which help quantify the 'sprayability,' 'printability,' and overall processability of a fluid. For example, ejecting a polymer solution with a long extensional relaxation time from a nozzle can result in filament formation and droplet retraction back into the nozzle, rendering it unsuitable for printing.[10–12] In spraying polymer solutions, the mean droplet size has been shown to increase with extensional relaxation time.[13]

Due to the similarity of fluid dynamics involved, capillary thinning-based measurements are often used to evaluate the processability of fluids in processes dominated by extensional flows.[14] In these measurements, a liquid bridge is formed between two surfaces. The liquid bridge then undergoes self-thinning and breakup, which is typically driven by inertial and surface tension forces and resisted by viscous forces.[14] In polymer solutions, a cylindrical filament often forms prior to breakup as elastic forces also resist filament thinning. Thus, several relevant

[a]Department of Chemical Engineering and Materials Science, University of Minnesota, Minneapolis, MN 55455, USA. Tel: +1 612 625 2551; *E-mail: mcalab@umn.edu

† Electronic Supplementary Information (ESI) available. See DOI: 10.1039/cXsm00000x/

parameters governing thinning include fluid density ρ, surface tension σ, and zero-shear viscosity η_0. To determine the dominant forces and relevant flow regime, the dimensionless Ohnesorge number compares the viscous forces to inertial and surface tension forces acting on the fluid:[14]

$$Oh = \frac{t_{vc}}{t_R} = \frac{\eta_0}{\sqrt{\rho \sigma R_0}} \quad (1)$$

where R_0 is the initial radius of the fluid filament. Here, $t_{vc} = \eta_0 R_0/\sigma$ is the timescale governing viscocapillary (VC) thinning ($Oh > 1$), common in more viscous fluids, and $t_R = \left(\rho R_0^3/\sigma\right)^{1/2}$ is the characteristic timescale for inertio-capillary (IC) thinning ($Oh < 1$), also known as the Rayleigh time. Once dominant thinning regimes are determined, the temporal evolution of the minimum filament radius can be analyzed to yield quantitative extensional rheological parameters and timescales, which reflect the processability of a material via methods dominated by extensional flow.

Capillary breakup extensional rheometry (CaBER) is a commercial technique that is often used to measure and analyze fluid pinching dynamics. CaBER forms the liquid bridge by imposing an initial step strain on fluid filled between two plates. Unfortunately, this method of generating the liquid bridge causes several problems that limit the types of fluids that can be measured. The step stretch often occurs on timescales longer than the breakup time of low-viscosity fluids, resulting in breakup of the liquid bridge before the plates can reach full separation.[15–18] Additionally, the step stretch can induce unwanted inertial effects into the thinning filament and disrupt underlying microstructure in the test fluid, resulting in lower measured extensional viscosities and extensional relaxation times.[19–21] The slow retraction method (SRM)[17] and custom CaBER instruments with faster plate separation times[22] have been used to enable the technique to measure fluids with lower viscosity than previously possible. However, the plate separation in faster CaBER instruments can still perturb underlying microstructures in the fluid, and the filament formed in SRM tends to be very slender before the measurement even begins, precluding observation of the full filament lifetime.

Recently introduced by Dinic and Sharma,[16] Dripping-onto-Substrate (DoS) extensional rheometry has addressed some shortcomings of the CaBER technique, enabling the characterization of low-viscosity ($\eta_0 < 20$ mPa·s), low-elasticity ($\lambda_E < 1$ ms), and low surface tension ($\sigma < 30$ mN/m) fluids such as dilute polymer solutions and protein solutions.[16,23,24] In DoS rheometry, a single droplet is slowly extruded from the end of a nozzle. The droplet then contacts a substrate, forming a liquid bridge that undergoes capillary-driven thinning and breakup. Due to the absence of a plate separation step and the use of a low extrusion rate, DoS rheometry is capable of measuring fluids with shorter relaxation times than is possible with CaBER.[16,25–27] Moreover, predeformations like those induced by step strains are minimized, enabling the measurement of a wider class of microstructured fluids and the determination of structure-flow relationships.

As the DoS technique was pioneered less than one decade ago, one major limitation is that DoS measurements are limited to ambient temperatures. Recently, researchers have created closed chambers[28] or chambers with solvent reservoirs[23] to enable DoS measurements in volatile solvents. However, a temperature control chamber has yet to be incorporated into DoS rheometry, whereas heated CaBER has been developed both commercially and via custom design.[22,29,30] In commercial CaBER instruments, the two end plates are heated and cooled by circulating fluid, and the measurement cell is enclosed within a double cover. Consequently, commercial CaBER instruments can be used to measure solution extensional rheology at temperatures between 0 and 60 °C, albeit with limited temperature accuracy given that only the plates are heated. Additionally, the measurement cell is not well-sealed, as shown recently in measurements of volatile polymer solutions.[23]

Custom CaBER instruments have made advances in temperature-controlled capillary thinning measurements. To measure the extensional rheology of polycarbonate melts, Sur *et al.*[29] constructed a high-temperature CaBER wherein the sample environment was enclosed in an oven that could reach temperatures up to 400 °C. To measure the extensional rheology of motor oils, Du *et al.*[22] constructed a customized CaBER in which the two endplates were enclosed in an acrylic chamber and heated using resistance heating modules that can maintain a temperature up to 250 °C. Most recently, Van Aeken *et al.*[30] constructed a CaBER-based instrument with a brass fluid bath to enable horizontal extensional measurements in an external fluid; to conduct measurements at elevated temperatures, the brass frame can be heated via cartridge heaters. In contrast, in DoS instrumentation introduced by Dinic *et al.*[16] and used by many others,[31–34] the sample is exposed to the environment and lacks heating elements. Thus, temperature-controlled extensional measurements are commonly accessible using CaBER instrumentation, but no developments to-date have been made towards temperature-controlled DoS measurements. Consequently, measuring the extensional rheology of low viscosity, low elasticity fluids or volume-limited samples – instances in which DoS is the preferred technique – has largely been limited to ambient temperatures.

While CaBER has previously been used to measure the extensional rheology of self-assembled systems like wormlike micelles (WLMs), several studies have demonstrated that the extracted rheological parameters are dependent on the instrument operating parameters.[20,21] WLMs are long, flexible structures formed by the temperature-dependent self-assembly of amphiphilic molecules, which are typically small molecule ionic surfactants. As WLMs are known to rapidly break and recombine at equilibrium and under flow, the self-assembled microstructure is, unsurprisingly, highly sensitive to the rapid deformation imposed during the CaBER step stretch. Miller *et al.*[20] showed that the measured extensional viscosity and extensional relaxation time of CPyCl/NaSal WLMs strongly depend on step-strain magnitude and imposed extension rate. Additionally, Omidvar *et al.*[32] reported differences between DoS and CaBER measurements of the same extensional rheology parameters in CPyCl/NaSal and OTAB/NaOA WLMs. The results of both studies imply that the step strain in CaBER experiments causes micellar breakage that results in different measured extensional rheology. Because the liquid bridge in DoS rheometry is formed by slow droplet dis-

pensing rather than a step strain, the DoS technique can alleviate the issues associated with measuring WLMs via CaBER. However, because DoS rheometry is still a relatively new technique, only a handful of prior studies have used this method to examine WLM flow behavior.[27,31,32,35–37]

Many studies of WLM flow behavior and dynamics occur at elevated temperatures,[38–40] which must exceed the Krafft point to ensure surfactant solubility.[41] Additionally, WLMs exhibit a range of temperature-dependent flow behaviors and temperature-sensitive flow instabilities.[39,42] However, most studies on WLMs in extensional flow using CaBER (or DoS) have been performed at ambient conditions,[21,32,36,43,44] potentially due to the limited temperature accuracy of the CaBER instrument. Accordingly, an understanding of the temperature-dependent capillary thinning behavior and potential instability formation is lacking. While most WLMs form from small molecules, WLMs can also form from polymeric amphiphiles,[45] which are typically one to two orders of magnitude larger in molecular weight. However, to our knowledge, there are no reports on capillary-driven thinning in polymeric WLM solutions; thus, any potential differences between extensional flow behavior in conventional small-molecule WLMs and that in polymer WLMs are unknown.

To overcome temperature limitations in assessing sprayability and printability using the DoS technique, we developed temperature-controlled DoS (TC-DoS) rheometry, with a measurement accuracy of $\pm$ 0.5 °C, for the first time. The sample environment employs heaters for the nozzle, substrate, and enclosure to heat both the sample and the environment, distinguishing our instrument from commercial and custom CaBER chambers that only heat the endplates[22] or only heat the sample environment.[30,46] We characterize the temperature-dependent extensional behavior of a model system consisting of 4% wt poly(ethylene oxide)-*b*-poly(propylene oxide)-*b*-poly(ethylene oxide) (poloxamer 234, i.e. P234) in 0.9 M NaF, which forms spherical micelles at room temperature that elongate into WLMs at elevated temperatures. The choice of specific poloxamer solution and salt concentration were motivated by the following factors: (1) the self-assembled structure is highly sensitive to temperature; (2) the structural transitions are well-characterized; (3) solution extensional viscosity and relaxation time, among other parameters, are expected to change substantially with temperature, and (4) the thinning dynamics of the system are on the order of seconds – in contrast to other poloxamer systems wherein dynamics can occur on the order of minutes to hours – which enables measurements on reasonable timescales.[45] Using TC-DoS, we characterize the dramatic differences in the extensional behavior of P234 solutions over small temperature windows, covering inertiocapillary through elastocapillary thinning behavior. These proof-of-concept measurements and comparisons to prior studies using CaBER demonstrate the significant advantages of TC-DoS rheometry for measuring self-assembled fluids at elevated temperatures and, for the first time, provide insights into the extensional flow behavior of nonionic polymer WLMs.

2 Materials and Methods

2.1 Materials

D_2O (99.9% mol D, Sigma-Aldrich), poloxamer 234 (Synperonic PE/P84, Sigma Aldrich), and NaF ($\geq$ 99%, Sigma Aldrich) were used as received. Solutions of 4% wt P234 in 0.9 M NaF were prepared as done in our prior work.[45] Briefly, salt was first dissolved in D_2O, then poloxamer was added and stirred at 4 °C for 12 hrs until fully dissolved. D_2O was used as the solvent in the experiments herein to enable direct comparisons to results from our prior work, which used D_2O to improve contrast in neutron scattering measurements. Before DoS measurements, previously dissolved P234 solutions were placed on the shaker under refrigeration for at least 4 hours to ensure sample homogeneity.

2.2 Shear rheology

Oscillatory and steady shear rheology was performed on an Anton Paar MCR 302 stress-controlled rheometer. A 26.7 mm double gap concentric cylinder geometry was used to enhance torque signal because ambient solutions are low viscosity. Steady shear viscosities were used as an indicator of WLM growth with increasing temperature, as previously done.[45] Given the low shear viscosities at temperatures below the P234 sphere-to-rod transition,[45] a specific shear rate protocol was used to enhance signal at lower temperatures: a shear rate of $\dot{\gamma} = 10$ s^{-1} was used from 20 – 30 °C, $\dot{\gamma} = 1$ s^{-1} for 30 – 32 °C, $\dot{\gamma} = 0.1$ s^{-1} for 32 – 35 °C, and $\dot{\gamma} = 0.01$ s^{-1} for above 35 °C. The zero-shear viscosities used to calculate *Oh* for P234 at T = 23, 33, and 35 °C were estimated from these steady shear measurements.

Given the higher solution viscosities, creep measurements (σ = 0.2 Pa) were used to determine the zero-shear viscosities η_0 of the cylindrical and worm-like micelles at 37 °C and 39 °C. At the same temperatures, the longest shear relaxation times were determined via frequency sweeps. In the rheometer, the sample was brought up to and then held at the target temperature until a steady state response to oscillatory shear was achieved, after which frequency sweeps were performed. For all measurements at elevated temperatures, a solvent trap was used to mitigate evaporation. All shear rheology measurements were performed in triplicate, and results are reported with 95% confidence intervals.

2.3 Ambient DoS rheometry

Ambient ($T = 23 \pm 0.5$ °C) filament thinning dynamics and extensional rheology experiments were conducted using the low-volume DoS instrumentation described previously by Lauser *et al.*[24]. Briefly, a syringe pump was used to form droplets at the end of an 18 gauge (OD = 1.27 mm, ID = 0.84 mm) blunt tip nozzle using a flow rate of 164 μL/min, after which the syringe pump was turned off. Measurements were taken via the 'stationary drop' approach,[24] where a partially-wetting ($\theta < 90°$) glass substrate is slowly raised to contact the hanging droplet to minimize inertial effects. The droplet was backlit using a cool white bulb and a diffuser. A Chronos 1.4 high-speed camera was used to take videos of filament thinning with a frame rate of 11,806

frames per second (fps). Using ImageJ,[47] images were resized to achieve subpixel resolution and binarized for edge detection. A custom MATLAB code was then used to process the images and generate radius evolution curves based on the minimum filament radius R_{min}. For comparison across different materials, trials with sessile drop contact angles between 60 – 70° in the frame prior to filament breakup were used to minimize confounding effects from spreading on the substrate. The aspect ratios, $AR = H/2R_0$, of trials were 2-3 (Figure 1b). At least five trials ($N \geq 5$) were used to calculate average values and 95% confidence intervals of extracted rheological parameters.

2.4 Temperature-controlled DoS rheometry

To visualize filament thinning dynamics and measure extensional rheology at elevated temperatures, a custom temperature control chamber was constructed (Figure 1) and integrated into the native DoS instrumentation. The chamber consists of acrylic walls to isolate the sample environment and foam core insulation to minimize heat loss from the chamber to the surroundings and thus enable better temperature control. Inside the chamber, a nozzle heater and substrate heater keep the test fluid at the desired set point temperature. The substrate and needle heaters alone were insufficient for keeping the extruded fluid at the set-point temperature during droplet formation and filament thinning, so an enclosure heater warms the gap between the substrate and needle to reduce temperature gradients between the fluid droplet and chamber air (see SI.1 for validation and multivariate analysis of rheological and temperature parameters). All heating elements are controlled using customized proportional-integral-derivative (PID) control programmed onto an Arduino UNO microcontroller with a maximum measurement accuracy of $\pm$ 0.5 °C. Because the substrate was enclosed in a chamber in TC-DoS experiments, the substrate was set at a fixed height, fluid was extruded from the nozzle at a rate of 164 uL/hr, and the pump was turned off before the droplet contacted the substrate and underwent capillary-driven thinning. To capture temperature-dependent filament thinning behavior, high speed videos were taken using frame rates between 200 and 11,806 fps; lower frame rates were used for samples with longer breakup times and higher elasticity to enable higher resolution, which better captures the thin filament before breakup. Similar to ambient condition experiments, trials that reach sessile drop contact angles $\theta < 70°$ and $2 < AR < 3$ were used for analysis. At least five trials ($N \geq 5$) were used to calculate average values and 95% confidence intervals for rheological parameters at each temperature.

2.5 Surface tension measurements

Turning the pump off before the droplet contacts the substrate during ambient and TC-DoS measurements creates a stable pendant drop that enables the determination of surface tension. Pendant drop profiles were analyzed using the Pendent Drop plugin[48] in ImageJ that fits the droplet shape to the Laplace equation, from which surface tension values σ can be extracted. To validate this method of surface tension measurement, D_2O surface tension values were measured as a control. Under ambient conditions (T = 23 °C), the experimental value measured herein $\sigma = 69.2 \pm 1.5$ mN/m within 95% confidence was comparable to the value of σ = 71.9 mN/m (T = 25 °C) previously reported in the literature.[49]

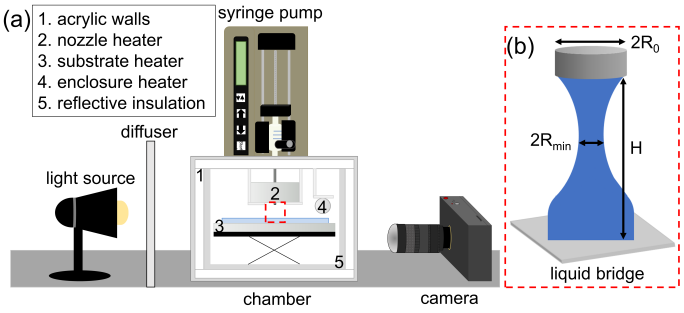

Fig. 1 Temperature-controlled DoS rheometry instrumentation. (a) The imaging system consists of a light source, diffuser, and high-speed camera. The temperature-control chamber enables heated measurements. A syringe pump dispenses fluid out of a nozzle to form a liquid bridge, shown in (b).

3 Results

The P234 system with added NaF was chosen due to its well-documented structural transitions with increasing temperature over fine temperature increments,[45] illustrated in Fig. 2; conditions measured with TC-DoS are indicated with unique symbols. While the shear viscosity, η, begins increasing beyond the sphere-to-rod transition temperature (~30 °C), noticeable increases in η do not occur until ~35 °C. Above 35 °C, the shear viscosity monotonically increases as the micelle elongates and entangles until a maximum viscosity is reached around 42 °C. After the viscosity maxmimum, the WLMs aggregate and phase separate, resulting in the precipitous drop in shear viscosity.[45] The extensional rheology measurements herein are taken up to ~ 40 °C to remain below well below the cloud point. The temperature-dependent changes in micelle structure and solution shear viscosity result in distinct extensional behavior, as discussed below.

3.1 Temperature-dependent capillary thinning of spherical and rod-like micelles

At ambient temperatures (23 °C), P234 solutions of low-shear viscosity spherical micelles exhibit distinct thinning phenomena from D_2O controls. For D_2O, $Oh \ll 1$ (Table 1), which indicates that thinning is dominated by inertial rather than viscous forces. Thus, just as in pure water,[24,27] D_2O thinning behavior can be described by the inertiocapillary (IC) scaling with a power law exponent $n = 2/3$:[26,50,51]

$$\frac{R_{min}(t)}{R_0} = \alpha \left(\frac{t_b - t}{t_R} \right)^{\frac{2}{3}} = \alpha \left(\frac{t_b - t}{\sqrt{\rho R_0^3/\sigma}} \right)^{\frac{2}{3}} \quad (2)$$

Here, $R_{min}(t)/R_0$ is the normalized minimum radius, t_b is the inviscid fluid breakup time, and α is a prefactor that typically ranges from 0.4 to 1.[14,16,52–55] As expected, when the ambient temperature D_2O minimum radius evolution is plotted on a log-log scale and shifted by the breakup time t_b (Figure 3b), a linear profile

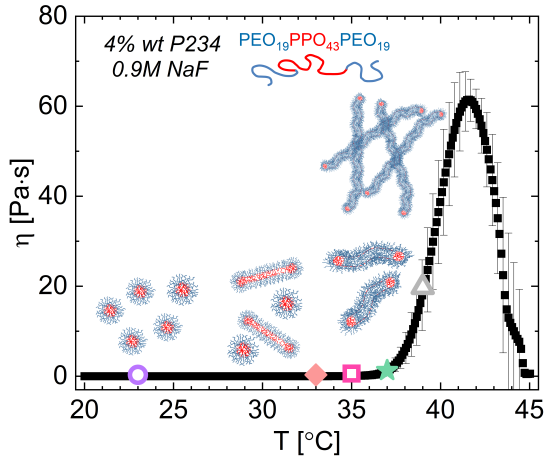

Fig. 2 Low shear rate viscosity η with temperature for P234 in 0.9M NaF; see Sec. 2.2 for shear protocol and SI.7 for data on a log-linear scale. Spherical micelles transition to rods (coexisting with spheres) near 30 °C. Above 35 °C, micelles elongate and increase η until a maximum η near 42 °C.[45] Error bars reported for every other point for clarity.

results with a slope of $n = 0.66 \pm 0.02$, corresponding to a power law exponent of 2/3 characteristic of IC thinning behavior. Moreover, the D_2O liquid bridge forms a distinct conical shape before pinch off, which is characteristic of such inviscid fluids (Figure 3c).[50,51,56]

Similar to D_2O, P234 solutions at 23 °C also exhibit IC thinning ($n = 0.66 \pm 0.01$) as expected ($Oh \ll 1$, Table 1), and the filament shape is also conical prior to break-up (Figure 3c). However, despite similar liquid bridge shapes throughout thinning between P234 and D_2O at 23 °C, the breakup time t_b for P234 is longer than that of pure D_2O (Table 1). Because surface tension forces dominate IC thinning (Eq. 2), the surface tensions for each fluid extracted from pendant drop analysis (Sec. 2.5) were used to rationalize the difference in t_b. The surface tension of pure D_2O measured over multiple trials is $\sigma = 69.2 \pm 1.5$ mN/m, whereas the surface tension of P234 is $\sigma = 30.6 \pm 0.2$ mN/m. The surface tension of P234 solutions is reduced to 40% of the pure D_2O values due to the presence of P234 at the air-liquid interface. Similar to observations by Lauser *et al.*[24] in poloxamer 188 (P188) solutions,[24] the weaker surface tension forces in P234 must account for the longer t_b compared to that of D_2O at 23 °C because the other parameters (R_0, ρ) in the characteristic IC timescale t_R are virtually identical between P234 and D_2O. The calculated IC prefactor[24] for P234 solutions at 23 °C, $C_{calc} = 0.6\left(\frac{\sigma}{\rho R_0^3}\right)^{1/3}$ (Table 1), also agrees well with the prefactor extracted from the fit (C_{fit}, Table 1), further confirming the suitability of an IC-based analysis and the influence of fluid surface tension on t_b.

Breakup times and power law exponents describing P234 thinning behavior increase monotonically with increasing temperature from 23 °C to 33 °C and finally 35 °C (Table 1), reflecting the growth of spherical micelles into rod-like micelles above the sphere-to-rod transition temperature ~30 °C.[45] The breakup time increases from $t_b = 5.1 \pm 0.1$ ms at 23 °C to 7.5 ± 0.2 ms at 35 °C. Concomitantly, the power law exponent n that describes all or part of P234 thinning behavior deviates from the IC scaling of 2/3 as temperature increases. Linearizing and then fitting the 33 °C and 35 °C P234 thinning profiles to $R_{min}/R_0 \sim t^n$ yields increasing power law exponent values of $n = 0.70 \pm 0.01$ at 33 °C and 0.84 ± 0.04 at 35 °C. Unsurprisingly, Oh also increases, suggesting that viscous forces become increasingly dominant during filament thinning (Table 1). The filament shapes also reflect a deviation from IC thinning; the conical shape seen in P234 at 23 °C gradually becomes more slender and elongated in the frames prior to break-up (Figure 3).[57] The same trends in t_b and n have been observed in other polymer systems, albeit with increasing concentration rather than temperature. For example, the evolution of n from 2/3 to 1 as Oh increases from $Oh \ll 1$ to $Oh \approx 1$ has also been observed with increasing concentration in solutions of high molecular weight PEO.[16,26] Additionally, the increase in n and t_b with temperature in P234 is analogous to the increase in the same parameters in P188 solutions with increasing concentration.[24]

Given that the surface tension of P234 remains relatively constant at ~30 mN/m regardless of temperature, the increase in

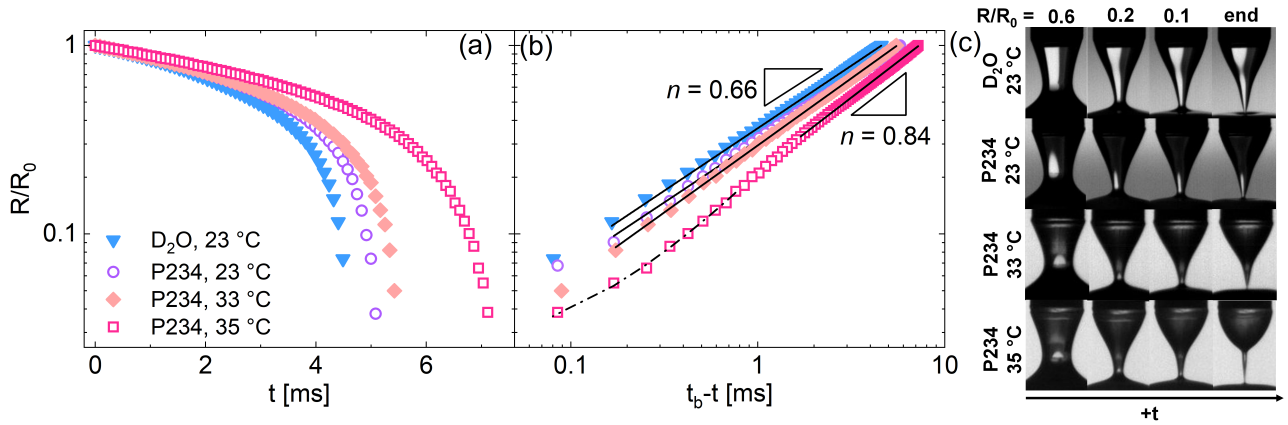

Fig. 3 Representative radius evolution curves and image sequences for D_2O (23°C) and P234 with increasing temperature up to 35°C. (a) Radius evolution curves for D_2O and P234 show increasing t_b and changes in curve shape with increasing temperature. Solid black lines denote power law fits, and dotted black lines denote Anna-McKinley model fits (Eq. 4). (b) Frames at matched $R/R_0 = 0.6$, 0.2, and 0.1 and just before breakup show that the filament becomes increasingly slender with increasing temperature.

t_b and n with increasing temperature is not a result of weakening surface tension forces but rather a result of increasing solution viscosity η caused by micelle lengthening (Figure 2). Consequently, as temperature increases, the power law thinning region evolves from IC behavior at 23 °C towards viscocapillary (VC) behavior, which is characterized by a linear scaling in the radius evolution according to the following model:[51,58,59]

$$\frac{R_{min}(t)}{R_0} = 0.0709\frac{\sigma}{\eta_0 R_0}(t_b - t) \quad (3)$$

The deviation from IC behavior with increasing temperature is further supported by the relative values of C (Table 1). C_{fit} strongly deviates from C_{calc} with ~75% difference as temperature is increased. The same deviation is seen in calculated and fit values of t_R (SI.4). Similar deviations in fit and calculated values of C and t_R have been observed as increasing polymer concentration causes deviations from IC thinning in P188 solutions.[24]

Notably, at 35 °C, P234 thinning behavior can no longer be described by a single model. The initial thinning behavior can be described by a power law scaling t^n, but the final stages of thinning before breakup (short $t_b - t$) deviate from linearity when plotted on a log-log scale (Figure 3b). Instead, the second thinning regime exhibits weakly elastic behavior, which manifests in the 2D images as a filament that is more slender and cylindrical than the IC conical shape just before breakup (Figure 3c). This weakly elastic thinning contrasts standard elastocapillary (EC) behavior, which manifests as a slender, cylindrical filament that is axisymmetric about the midplane. The 2D images and thinning behavior of P234 at 35 °C are remarkably similar to those of 200 mg/mL P188 (P188-200) reported by Lauser et al.[24] Both fluids exhibit similar Oh values of $O(10^{-1})$; however, the increase in Oh for P188-200 was attributed to an increased viscosity due to increased P188 content, whereas the increase in Oh for P234 at 35 °C is due to micelle growth, which increases solution viscosity. Even then, the filament shape in both P234 and P188 evolve from conical to more slender and cylindrical with increasing temperature and concentration, respectively.

Similar to concentrated P188 solutions, the weakly elastic thinning regime of P234 at 35 °C can be fit using the semi-empirical model proposed by Anna and McKinley:[60]

$$\frac{R_{min}(t)}{R_0} = A\exp(-Bt) - Ct + D \quad (4)$$

The fitting parameter B is related to the extensional relaxation time λ_E of the cylindrical micelles ($B \approx 1/3\lambda_E$), and C can be used to determine the steady, terminal extensional viscosity ($C \approx \sigma/2\eta_{E,\infty}R_0$).[25,60] Finally, the elastic filament lifetime t_E, which roughly corresponds to the duration of weakly elastic regime, can be determined from D/C.[61] Eq. 4 has been used previously to fit weakly elastic behavior in surfactant WLM solutions.[20,32,43,62,63] A fit to the end of thinning for P234 at 35 °C yields an extensional relaxation time $\lambda_E = 2.1 \pm 0.1$ ms and a reasonable elastic filament lifetime of $t_E = 2.6 \pm 0.2$ ms, which reflect the short, elastic effects of rod-like micelles in solution.

3.2 Temperature-dependent capillary thinning of cylindrical micelles

At 37 °C, the elasticity of P234 solutions becomes even more pronounced due to micelle lengthening. Linear viscoelastic (LVE) shear rheology measurements at 37 °C exhibit a single crossover between the storage modulus G' and loss modulus G'', suggesting this system can be fairly well-described by a single relaxation mode of shear relaxation time $\lambda_s = 1.2$ s (Figure 4a). Calculations based on the LVE rheology and scaling relationships[64] allow the micelle contour length at 37 °C to be estimated as approximately 400 nm (SI.8). However, these calculations are likely an overestimate of the true contour length due to the absence of a true plateau modulus, G_0, or minimum in G'' (Figure 4a); calculations are instead performed based on inflection points reminiscent of these features (see SI.8). Based on these features from the LVE rheology and estimates of the relevant length scales, micelles at this temperature are likely wormlike, but not highly entangled.

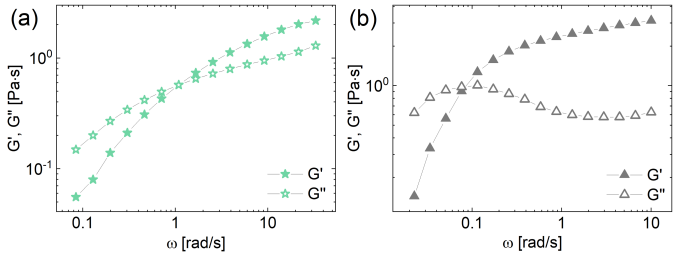

Fig. 4 Frequency sweeps for P234 at (a) 37 °C and (b) 39 °C reflect increasing WLM growth and entanglement with increasing temperature.

The radius evolution curve of the micelles at 37 °C exhibits a distinct elastocapillary (EC) thinning regime, indicated by the characteristic linear region on a semi-log scale. A thin, cylindrical filament characteristic of EC behavior is also present throughout the thinning process (Figure 5a). When the relaxation behavior can be described well by a single relaxation mode, as is common for polymer solutions, the EC thinning region can be fit to the following model:[14,15,65]

$$\frac{R_{min}(t)}{R_0} \approx \left(\frac{G_E R_0}{2\sigma}\right)^{\frac{1}{3}} \exp\left(\frac{-t}{3\lambda_E}\right) \quad (5)$$

where G_E is the apparent extensional modulus. From Eq. 5, the longest relaxation time λ_E can be extracted, where the $\left(\frac{G_E R_0}{2\sigma}\right)^{1/3}$

Table 1 Shear and extensional rheology parameters extracted from images and radius evolution curves for pure D_2O and P234 solutions that exhibit IC through EC thinning. Uncertainties are reported as 95% confidence intervals.

sample	T [°C]	σ [mN/m]	η_0 [Pa·s]	C_{fit}	C_{calc}	Oh	n	t_b [ms]	λ_s [s]	$\lambda_{E,I}$ [s]	$\lambda_{E,III}$ [s]	η_E^∞ [Pa· s]
D_2O	23.0 ± 0.5	69.2 ± 1.5	1.1 ·10^{-3}	35.1 ± 4.1	37.6	4.9 ·10^{-3}	0.66 ± 0.02	4.4 ± 0.2	-	-	-	-
P234	23.0 ± 0.5	30.6 ± 0.2	2.0 ·10^{-3}	30.1 ± 1.1	28.6	1.4 ·10^{-2}	0.66 ± 0.01	5.1 ± 0.1	-	-	-	-
P234	32.8 ± 0.2	29.4 ± 0.1	3.0 ·10^{-3}	37.3 ± 3.1	28.3	2.1 ·10^{-2}	0.70 ± 0.01	5.5 ± 0.2	-	-	-	-
P234	34.7 ± 0.1	29.4 ± 0.3	3.4 · 10^{-2}	63.8 ± 11.8	28.3	2.5· 10^{-1}	0.84 ±0.04	7.6 ± 0.2	-	(2.1 ± 0.04)· 10^{-3}	-	0.30 ± 0.03
P234	37.1 ± 0.1	30.0 ± 0.4	1.5 ± 0.8	-	-	1.1· 10^{1}	1.03 ± 0.02	-	1.2 ± 1.0	(25 ± 6) ·10^{-3}	-	15 ± 5
P234	39.2 ± 0.4	29.0 ± 0.4	25.0 ± 7.2	-	-	1.8 ·10^{2}	1.05 ± 0.05	-	11.7 ± 1.6	8.4 ± 3.0	18.6 ± 2.3	6780 ± 1120

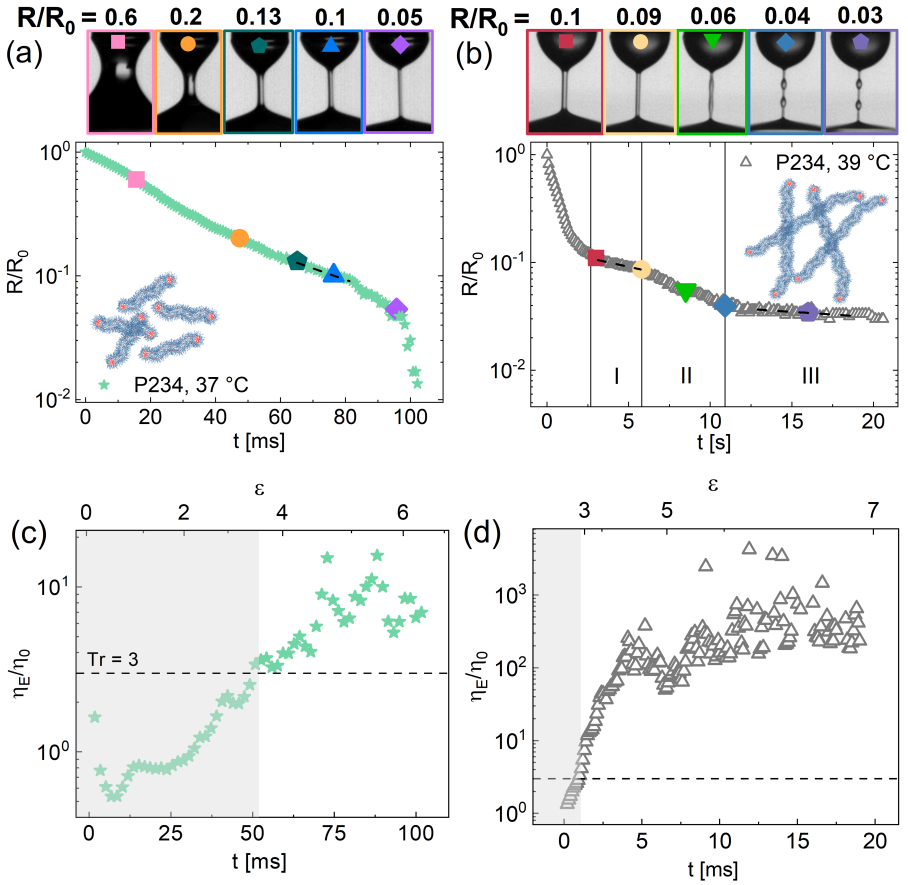

Fig. 5 Radius evolution curves for P234 at (a) 37 °C and (b) 39 °C reflect pronounced elasticity. Dotted black lines denote EC fits to Eq. 5. Corresponding Trouton ratios, $Tr = \eta_E/\eta_0$, as a function of time and accumulated strain are shown in (c) 37 °C and (d) 39 °C. Dotted horizontal line denotes Newtonian value of $Tr = 3$. Shaded region denotes thinning prior to the EC regime, where Eq. 6 does not apply.

prefactor is typically treated as a fitting constant.[16,24] At 37 °C, the extensional relaxation time was determined as $\lambda_E = 30 \pm 11$ ms (see SI.2 for data from all trials), which is one order of magnitude greater than the relaxation time of P234 at 35 °C (Table 1). The extensional relaxation time is two orders of magnitude smaller than the shear relaxation time ($\lambda_E/\lambda_s \ll 1$). Sachsenheimer *et al.*[40] attribute differences in the WLM shear and extensional relaxation time of this magnitude to micelle stretching and orientation in extension rather than breakage. However, given the reported uncertainty in temperature in the TC-DoS trials, and that the shear viscosity near 37 °C is highly sensitive to small changes in temperature (Figure 2), we refrain from further analyzing these differences in relaxation time.

At 39 °C, the WLMs elongate further, resulting in much slower dynamics and more pronounced elasticity than for the WLMs at 37 °C. A clear plateau modulus and a distinct minimum in G'' appear in shear LVE measurements (Figure 4b), indicating the presence of numerous entanglements. Here a single crossover in the dynamic moduli is observed, yielding a shear relaxation time, $\lambda_s = 11.7$ s, that is an order of magnitude larger than that at 37 °C. The elastocapillary regime in P234 at 39 °C reproducibly exhibits three distinct thinning regions (Figure 5b), from which two different extensional relaxation times can be extracted (Table 1). In region I, WLMs undergo pure EC thinning, corroborated by the characteristic cylindrical filament shape and the fit to Eq. 5. Here, the observed filament width is uniform over the entire filament length (Figure 5b, images 1-2). Over the length of region II, the beads-on-a-string (BOAS) instability – a series of beads connected by axially symmetric filaments – gradually forms (image 3, Figure 5b). Finally, in region III, the filament connecting the beads undergoes thinning. As shown in Figure 5b (images 4-5), two distinct, equal-sized beads form which then slowly migrate in opposite directions until the filament breaks up. The thinning in region III is also exponential and can be described by Eq. 5; the stages of bead formation and subsequent filament thinning are consistent with numerical simulations[66–68] and prior experiments on aqueous PEO solutions.[17,69–71] Notably, the regions in P234 WLMs are exceptionally well-defined due to the slow dynamics relative to PEO solutions.

Fitting region I to Eq. 5 yields an extensional relaxation time $\lambda_{E,I} = 8.4 \pm 3.0$ s, and fitting region III yields $\lambda_{E,III} = 18.5 \pm 2.3$ s (Table 1). Even though WLM contour length approximately doubles from 37 °C to 39 °C (SI.8), both $\lambda_{E,I}$ and $\lambda_{E,III}$ at 39 °C are multiple orders of magnitude greater than λ_E at 37 °C. However, both $\lambda_{E,I}$ and $\lambda_{E,III}$ are comparable to λ_s ($\lambda_s = 11.7$ s) such that $\lambda_{E,1}/\lambda_s \approx 1$, which agrees with the results reported by Sachsenheimer et al.[40] for fast-breaking surfactant WLMs. As demonstrated by the LVE rheology (Figure 4b) and our previous shear studies,[45] P234 WLMs at 39 °C are indeed fast-breaking; thus, the findings of Sachsenheimer *et al.*[40] regarding relaxation

time ratio appear applicable to nonionic WLMs.

As expected, the P234 WLMs at 37 °C and 39 °C exhibit VC thinning at early times (see SI.5). At these temperatures, the shear viscosity sharply increases due to micelle growth, resulting in $Oh \gg 1$ (Table 1). As such, the stronger viscous contribution to the initial thinning regime results in VC thinning behavior. Notably, when compared to sharp IC-EC transitions in dilute PEO solutions, VC-EC transitions in the semi-dilute WLM solutions herein are less distinct, i.e. the end of the VC and start of the EC regime are more difficult to define.[16,26,72] Similar gradual VC-EC transitions have been observed in semi-dilute and concentrated PEO solutions.[26]

3.3 Extensional viscosity of cylindrical and wormlike micelle solutions

For fluids exhibiting EC behavior, the apparent extensional viscosity can be determined using the radial decay in time:[14]

$$\eta_E \approx -\frac{\sigma}{2dR_{min}/dt} \tag{6}$$

Representative Trouton ratios, $Tr = \eta_E/\eta_0$, of P234 at 37 °C and 39 °C are plotted as a function of time and accumulated strain $\varepsilon = -2ln(R_0/R_{min}(t))$ in Figure 5c-d. In the initial thinning region prior to EC thinning, shaded in gray, the value of Tr lies below the Newtonian limit of 3 for all or part of the time; this apparent discrepancy is more pronounced at 37 °C than at 39 °C. The discrepancy in Tr values at early thinning times is likely a combination of experimental uncertainty, the validity of Eq. 6 in this region, and transient extensional thinning. First, any calculation of η_E assumes a slender filament, which is not satisfied at early thinning times. The apparent extensional viscosity in Eq. 6 is defined based on a force balance that includes viscous, elastic, and capillary contributions.[60] However, the initial thinning region is typically dominated by viscous or inertial forces and thus assumed to be void of elastic forces. Here, the gravitational forces can also be neglected based on sufficiently low Bond numbers, Bo, calculated for each sample (SI.6). As such, the determination of η_E in the early thinning region must be modified to give $\eta_E = -(X-1)\sigma/(2dR_{min}/dt)$, where X depends on filament shape and thus the dominant forces acting on the filament.[21,59] Depending on the similarity solution, the value of X can vary from ≈ 0.5 to 1.[59] However as discussed by Kim *et al.*[21], who also saw $Tr < 3$ in surfactant WLMs at early times during CaBER, viscous rearrangement of the upper and lower fluid reservoirs prior to formation of a long, predominantly cylindrical column likely impacts the radial evolution in this region, and thus Tr. These authors also saw qualitatively similar trends in Tr to those observed at 37 °C in some cases, where $Tr \approx 3$ at the start of thinning but then rapidly decreases and subsequently recovers with increasing strain; they attribute this behavior to transient extensional thinning from chain alignment.[21] As such, the Tr values in the shaded regions are included in Figure 5c-d for completeness, but they are not further analyzed. Considering Tr from the start of the EC regime corresponding to $\varepsilon \approx 3$ - 4 and beyond (unshaded regions, Figure 5c-d), Tr increases with increasing ε and thus reflects extensional hardening at both 37 and 39 °C. The Tr values also reach a maximum and plateau prior to break-up at both temperatures. This behavior has also previously been reported in extensional studies of surfactant WLMs.[31,32,43,44]

The Tr ratios reached at 39 °C are one order of magnitude higher than those reached at 37 °C. At 37 °C, the maximum Tr values Tr_{max} are $O(10^1)$, whereas Tr_{max} is $O(10^2)$ at 39 °C, suggesting that extensional viscosity η_E increases more rapidly than the zero-shear viscosity η_0 between 37 and 39 °C. Analogous to polymer solutions in which extensional viscosity and Tr increases with chain length,[73,74] the difference in Tr_{max} herein can likely be attributed to the longer contour length of WLMs at 39 °C compared to 37 °C.

3.4 Beads-on-a-string instabilities

The BOAS instability formed reliably in DoS measurements of P234 WLMs at 39 °C; in contrast to dilute PEO solutions that rapidly form multiple bead generations,[69,75] here a single generation is observed. Figure 6 depicts the formation (region II) and evolution (region III) of BOAS instabilities at similar t/t^* values across representative trials, where t^* denotes the end of each BOAS region. Three distinct BOAS behaviors are observed in region II, corresponding to the formation of: two stable beads, three beads that coalesce into two beads, and three or more stable beads (Figure 6a, top to bottom). However, while the number of beads varies ($N = 2-5$), the stage of bead formation and thinning is similar at each t/t^*, reflecting the reproducibility of the BOAS phenomenon in this system. As determined by multivariate analysis (see SI.10.1), the observed number of beads is strongly, linearly correlated with aspect ratio (H/R_0) and filament length. However, the number of beads is neither correlated with the time-width of regions II or III, nor with the extensional relaxation time in either region, suggesting that the observed behavior is largely due to geometrical effects. As expected, the aspect ratio and filament length are also not correlated with the extensional relaxation times or region time-widths (SI.10.1), implying that the measured extensional rheology timescales are independent of both bead number and instrument parameters within this operating window. Finally, perhaps unsurprisingly, the average liquid volume per bead decreases with increasing bead number (SI.10.3); an obvious difference in bead size can be discerned between the two-bead vs. four-bead cases (Figure 6, row i vs. iv).

At early times in region II (Figure 6a, frames 1-2), bead formation begins with the onset of pinching in the 'neck' regions where the filament connects to the upper and lower fluid bulb. As the instability evolves, discrete beads form between the neck regions (Figure 6a, frames 2-3), consistent with previous simulations.[66–68,76] In the filament between the neck regions, pinching occurs between the growing maxima in filament radius as the instability progresses, resulting in a first generation of beads with similar sizes. The filament radius remains slightly wider between beads than in the neck region until the beads have fully formed, and similar to observations from experiments and simulations,[66,69] the bead diameter exceeds the initial filament radius once fully formed. At later times, the neck regions gradu-

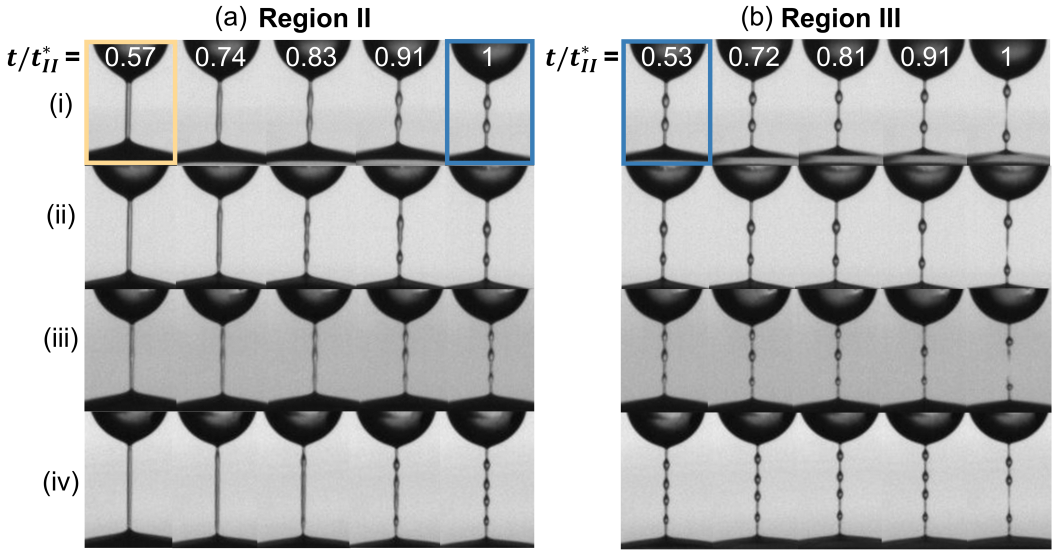

Fig. 6 Representative beads-on-a-string instabilities that form in P234 solutions at 39 °C. (a) Formation of relatively uniform beads on the fluid filament in region II of thinning. (b) Bead sizes stabilize while filament thinning continues between beads in region III. First and last frames in (a) and (b) correspond to the beginning and end of each thinning region. Rows correspond to (i) radius evolution data in Figure 5b with $N = 2$ beads, (ii) bead coalescence, (iii) $N = 3$, and (iv) $N = 4$. Numbers in white correspond to time normalized by end time of each region, t^*.

ally grow in length and the filament thins substantially (frames 3-5). By $t/t^*_{II} = 0.91$, discrete, stable beads have formed for $N = 2$ and $N = 3$, whereas beads do not fully form until the end of region II ($t/t^*_{II} = 1$) for the $N \geq 4$ cases. Interestingly, the middle bead merges with the upper bead prior to full bead formation in the lowest stability case (Figure 6a.ii); similar bead coalescence events were noted by Oliveira and McKinley[69] in aqueous PEO solutions. For additional analysis and discussion of the region II behavior and symmetry, see SI.10.2.

In region III, progression of the BOAS instability differs widely based on bead number and relative bead size. The trial with two equal-sized beads evolves most symmetrically and undergoes filament breakup at roughly the midpoint of the filament (Figures 6b.i, S16). In contrast, the two unequal bead sizes resulting from coalescence in region II cause filament rupture closer to the bottom bead and the bottom of the filament, $\sim 65\%$ of the way down from the top bulb (Figure 6b.ii). For most of this trial, the larger top bead travels significantly faster than the smaller bead (Table S9), reminiscent of how larger beads travel faster along conical fibers.[77] Interestingly, the symmetry of bead formation in region II does not always lead to a symmetric breakup event. While the four-bead trial is symmetric about the horizontal midplane at the end of region II (row iv, Figure 6), the top bead coalesces with the top bulb during thinning in region III, yielding an eventual breakup between the lower two beads occurring $\sim$65% of the way down the filament, much closer to the filament end.

The direction and speed at which the beads travel along the filament depend strongly on vertical position. Similar to observations by Oliveira and McKinley[69], beads near the top of the filament typically have a positive z-velocity and travel up the filament, whereas those near the bottom of the filament typically have a negative z-velocity and travel down the filament (Figures S16, S17). The direction of bead travel depends on its position relative to the location of breakup, z_{crit}; beads above z_{crit} have positive velocities while those below have negative velocities. For all trials with $N \geq 3$ in region III, bead travel leads to coalescence between the top bead and top bulb. The top bead typically exhibits the largest velocity magnitude throughout region III prior to coalescence. When coalescence occurs (vertical lines, Figures S16, S17), a discontinuity in the velocities of the remaining beads is observed, similar to that observed in prior work on PEO solutions.[69,70] Bead coalescence causes elastic recoil due to release of elastic tension;[69] thus, all remaining beads exhibit negative z-velocities immediately following the coalescence event. While beads above z_{crit} briefly travel down the filament following recoil, these beads quickly regain positive velocities before breakup.

Despite differences across behavior type, the beads on a given filament ultimately evolve to be approximately uniform in size prior to breakup, with diameters usually within $\sim$10% of each other (Figures 6b, S16). These beads all form roughly concurrently in region II (Figure 6a), suggesting a single generation of beads. These early stages of bead formation and evolution resemble those observed previously in dilute PEO solutions[69,71] and are consistent with several prior simulations[66–68,76]; however, notably PEO solutions also exhibit pronounced 'blistering' instabilities where four or more generations of beads subsequently form.[69,71] Interestingly, the size of the first generation beads in dilute PEO and P234 WLMs are comparable; Oliveira and McKinley[69] reported PEO beads of 110 μm diameter, while the average first generation bead diameter in P234 WLMs is $\sim$116 μm.

Chang *et al.*[76] originally presented four criteria based on dimensionless groups that must be met for BOAS to initially form and for subsequent generations of beads to appear. While the mechanism of the latter blistering instabilities is under debate,[66,71,76,78] here we focus on these criteria as related to BOAS formation. The relevant dimensionless groups, related to capillarity and elasticity, are defined here to enable comparison with prior work. The Weissenberg number $Wi = \lambda_E \eta_0 / \rho R_0^2$ is a measure of

solution elasticity, and the Ohnesorge number for the thread is defined in Eqn. 1. The solvent viscosity ratio, S, is the ratio of the solvent and zero-shear viscosities such that $S = \eta_s/\eta_0$. Finally, the parameter L^2 characterizes the WLM finite extensibility, where L is the ratio of the fully stretched chain length to the equilibrium chain length. As determined by Chang *et al.* [76], to observe BOAS phenomena, Wi should be large ($Wi \gg 1$) given that the interplay between elasticity and capillarity triggers bead formation.[66,76,79] Additionally, Oh should be of order unity; L^2 should be large ($L^2 \gg 1$), and S should be finite ($S \neq 0,1$) such that inertia can play a critical role in instability growth. Note that prior systems exhibiting BOAS phenomena have had $Oh = O(10^2)$, so this criterion is not strict.[69]

Despite that the P234 WLMs are substantially more viscous than prior systems that exhibited BOAS phenomena,[69,75] the P234 solutions herein generally satisfy the four criteria for BOAS formation. For P234 WLMs, $Oh = O(10^2)$ (Table 1) and $L^2 \approx 100$ (see SI.10.4). S in the P234 WLMs is nearly zero regardless of whether the viscosity of D_2O is used ($S \sim 10^{-5}$) or an Oldroyd-B model is fit to the LVE rheology ($S \sim O(10^{-3})$), which seems troublesome given that S should be between 0 and 1.[76] However, the S-criterion stems from the need for S and $1-S$ to be larger than Wi^{-1} to reach an analytical solution.[76] Here, although S is near-zero in P234 WLMs, S and $1-S$ are always at least an order of magnitude greater than Wi^{-1} (see SI.10.4 for calculations).

4 Discussion

4.1 Beads-on-a-string instabilities in polymer WLMs vs. other systems

P234 WLMs appear to exhibit less developed BOAS instabilities than in dilute, high molecular weight PEO solutions. Consistent with simulations,[66–68] beads initially form a geometric lemon shape and evolve to nearly spherical in dilute, aqueous PEO; however, this instability progression is more limited in the P234 WLMs, and the beads remain a geometric lemon shape throughout region III. Clear differences between the relevant dimensionless parameters in P234 WLMs and in the low viscosity PEO solutions measured by Oliveira and McKinley[69] are used to rationalize these differences in behavior. While S in P234 WLMs is four orders of magnitude smaller than in PEO solutions ($S = 0.14$[70]), S is one order of magnitude greater than Wi^{-1} for both systems. However, more substantial differences arise when the balance of elastic and capillary vs. viscous forces are compared between the two systems. In P234 WLMs, Wi is $O(10^5)$ due to the long relaxation time and relatively high zero-shear viscosity whereas $Wi = O(10^1)$ for PEO solutions due to the relatively low PEO solution viscosity. As defined by Chang *et al.* [76], the capillary number $Ca = \eta_0^2/\rho\sigma R_0$, which quantifies the relative importance of viscous drag vs. surface tension forces, is also multiple orders of magnitude higher in P234 WLMs ($O(10^4)$) than in PEO solutions ($O(10^{-2})$). When taken together, the relative contributions of elastic and capillary vs. viscous forces to the observed flow phenomena can be quantified by the elastocapillary number $Ec = Wi/Ca = \lambda_E\sigma/R_0\eta_0$.[14] While Wi and Ca are substantially higher for the P234 WLMs, the elastocapillary number for P234 WLMs ($Ec = O(10^1)$) is an order of magnitude lower than that for PEO solutions, where $Ec = O(10^2)$. Given that R_0 is essentially equal in both systems (~0.6 mm), and the surface tension of P234 WLMs is only two-fold lower than that of PEO solutions, the ratio of λ_E/η_0 contributes most to the observed differences in Ec. Here, λ_E/η_0 for P234 WLMs is one order of magnitude smaller than that for PEO solutions, reflecting that the relatively high η_0 of P234 WLMs dampens elastic effects to a greater degree compared to PEO solutions, resulting in the less developed bead shape observed in experiments. These findings are consistent with prior numerical simulations in which a sufficiently high solution viscosity precludes BOAS formation by stabilizing the jet or filament.[68,80] For additional discussion on BOAS evolution and blistering instabilities, see SI.10.5.

The BOAS formed in the nonionic polymer WLMs herein are similar to that previously observed in surfactant WLMs, albeit with a few key differences. Sostarecz and Belmonte[81] studied BOAS that formed in CPyCl/NaSal WLM filaments created by a falling pendant drop in a viscous Newtonian oil. Like the P234 WLMs herein, the surfactant WLMs formed an initial single generation of approximately uniform beads. However, the beads formed by CPyCl/NaSal WLMs in oil were much larger, with a bead diameter ~ 2 mm; in contrast, the beads formed by P234 WLMs have a diameter ~ 0.1 mm (see Figures S16, S17). Sostarecz and Belmonte[81] also reported the formation of secondary beads just prior to pinch-off in surfactant WLMs, which is also observed in the P234 WLMs at higher bead numbers (Figure 6b.iii-iv). Notably, the dynamics of CPyCl/NaSal WLMs in oil were much slower due to the density difference and viscosity of the surrounding oil;[81] their experiments lasted on the order of minutes, whereas the experiments herein last on the order of tens of seconds. As such, the surrounding oil enabled beads to form in the surfactant WLMs, whereas the instability in P234 WLMs was able to form in air. Interestingly, the shear relaxation time of the CPyCl/NaSal solution used by Sostarecz and Belmonte[81] was λ_s = 33 s, which is approximately three times longer than that of P234 at 39 °C (Table 1). Despite the faster dynamics of P234, BOAS in P234 WLMs were observable without a surrounding viscous fluid; thus, BOAS in this study may have been enabled by the minimal disruption of WLM structure by the DoS technique. Notably, Bhardwaj *et al.* [43] did not mention BOAS phenomena occurring in CaBER measurements of surfactant WLMs of similar composition to Sostarecz and Belmonte[81]. Instead, prior filament stretching[43,82] and pendant drop[83] experiments of surfactant WLMs in air reported premature filament rupture, which precluded the observation of BOAS instabilities.

4.2 Nonionic polymer WLM vs. surfactant WLM extensional rheology

To our knowledge, this study marks the first extensional rheology measurements of nonionic polymeric WLMs, whereas the extensional rheology of ionic surfactant WLMs has been studied via DoS, CaBER, and filament stretching extensional rheometry (FiSER). In the following section, the extensional flow behavior of entangled P234 polymer WLMs at 39 °C is compared to the behavior observed across the surfactant WLM literature. Note that while P234 and surfactant WLM extensional behavior are

directly compared here, previous extensional rheometry on surfactant WLMs was often conducted using filament stretching devices instead of DoS rheometry. The step-stretch deformation used to form the liquid bridge in CaBER can impact resulting measurements of λ_E and η_E, especially in microstructured fluids such as WLM solutions.[20,32] Thus, these comparisons to prior studies should be interpreted with caution. Nevertheless, Table 2 comprehensively summarizes the structural, shear, and extensional parameters of surfactant WLMs obtained from literature; this analysis is limited to only DoS, CaBER, and FiSER measurements. Note that while the molecular weight of P234 is ∼10x larger than the molar mass of each of the ionic surfactants, the cross-sectional radius of these WLMs is only three-fold larger than that of the surfactant WLMs (Table 2).

P234 WLMs at 39 °C can be most closely compared to two surfactant WLM systems based on contour length calculations (Table 2, SI.8): (i) 1.5% wt CTAT/SDBS with 0.01% wt NaTos (Calabrese and Wagner[38,84]), and (ii) 50/25 CPyCl/NaSal in NaCl brine (Bhardwaj *et al.*[43]). Both surfactant WLM solutions are expected to be composed of linear rather than branched micelles, just as in the P234 WLMs at 39 °C[38,40,45], and the three systems have similar contour lengths $L_c \approx 0.8$ μm. The linear 1.5% wt CTAT/SDBS WLMs have similar shear rheological parameters to the P234 WLMs at 39 °C; for example, the plateau modulus G_0, zero-shear viscosity η_0, and shear relaxation time λ_s are less than three-fold different between the two systems; the resulting extensional relaxation times λ_E are also on the same order-of-magnitude. The maximum Tr for the CTAT/SDBS surfactant WLMs is lower than that observed in the P234 WLMs ($Tr_{max} = 40$ vs. 270). However, the values are similar and could result from the slight differences in solution rheological parameters. For example, the ratio of the extensional and shear relaxation times, λ_E/λ_s, is of similar magnitude but is greater for the P234 WLMs; a higher λ_E/λ_s indicates more prominent extensional flow behavior and would likely increase Tr_{max} (see Sec. 4.3 below). Additionally, the difference in methodology (DoS vs. CaBER) likely plays a role. As shown by Omidvar *et al.*[32] (Table 2), extensional rheology parameters extracted from CaBER tend to be lower than those extracted from DoS, and the magnitude of the differences in Tr_{max} between the P234 and CTAT/SDBS WLMs is consistent with the magnitude of the differences in Tr_{max} from CaBER vs. DoS between trials on the same sample.[32] Unsurprisingly, these comparisons suggest that nonionic WLMs exhibit extensional hardening and relaxation similar to ionic surfactant WLM systems given similarities in the shear rheological behavior, despite the larger amphiphile molecular weight and micelle cross-sectional radius in P234 WLMs.

In the 50/25 CPyCl/NaSal WLMs, the shear rheology parameters differ more substantially from the P234 WLMs at 39 °C. Despite similar contour lengths and storage moduli (Table 2), both the shear and extensional relaxation times of the P234 WLMs are roughly two orders of magnitude greater than that of 50/25 CPyCl/NaSal WLMs. However, $\lambda_{E,I}/\lambda_s \approx 0.7$ for the P234 WLMs versus $\lambda_E/\lambda_s \approx 0.2$ for the CPyCl/NaSal WLMs. Surprisingly, Tr_{max} in the P234 WLMs is roughly half that in the 50/25 CPyCl/NaSal WLMs, despite that λ_E/λ_s is greater for the P234 WLMs and Tr from DoS are expected to be larger than from CaBER. Upon closer inspection, the LVE shear rheology for the 50/25 CPyCl/NaSal does not exhibit a true plateau in G' with increasing frequency,[43] suggesting deviations from ideal fast-breaking behavior. In fact, across linear surfactant WLMs (Table 2, refs. 32,36,43), the largest Tr_{max} are observed in solutions that do not exhibit a true plateau or show deviations from semi-circular behavior in the Cole-Cole representation of the LVE data. These observations are consistent with findings by Omidvar *et al.*[36] that noted a decreasing Tr_{max} as WLMs exhibited more Maxwellian LVE behavior. Deviations from fast-breaking behavior can occur due to slow breakage or due to the presence of short, rod-like micelles. In the latter case, the shorter rod-like micelles are not highly extensible, but rather large Tr_{max} are observed due to the low zero-shear viscosities.[36]

P234 WLMs at 39 °C also share some similar rheological features with fast-breaking 100/50 CPyCl/NaSal WLMs;[21] namely, L_c and η_0 are comparable. However, the 100/50 CPyCl/NaSal WLMs have a higher G_0, and both the shear relaxation time λ_s and extensional relaxation time λ_E are approximately one order of magnitude lower than those of P234 WLMs. However, these two WLM samples have comparable relaxation time ratios, λ_E/λ_s, which leads to comparable Tr_{max} (Table 2). Notably, this agreement in Tr_{max} depends heavily on the CaBER operating parameters, as Kim *et al.*[21] reported that the Tr_{max} in 100/50 CPyCl/NaSal WLMs ranged from $O(10^1)$ to $O(10^2)$ depending on aspect ratio. Unsurprisingly, lower Tr_{max} are observed for higher aspect ratios where the applied step strain is larger; better agreement in Tr_{max} is observed between the methods for smaller aspect ratios where the microstructure is less disrupted by the step strain. On the same 100/50 CPyCl/NaSal system, Bhardwaj *et al.*[43] reported a $Tr_{max} \approx$50 from CaBER measurements – equivalent to Tr_{max} from Kim *et al.*[21] at higher aspect ratios – and extension rate-dependent values of $Tr \approx$ 150-500 from FiSER measurements. Such method-dependent differences in Tr values complicate direct comparisons between extensional studies of WLMs and further highlight the nontrivial effects of the step-stretch pre-deformation in CaBER measurements of WLMs. On this front, DoS is advantageous because it enables measurements of temperature-dependent extensional behavior without significant pre-deformation in the form of a step-stretch or high extrusion rate.[26]

4.3 Liquid bridge extensional rheology methods for measuring self-assembled fluids

As aforementioned, direct comparison between P234 WLMs and previously-measured surfactant WLMs is difficult due to the use of different instrumentation (DoS, CaBER, and FiSER) and different instrument parameters within each method. In CaBER experiments, instrument parameters that affect the initial step-stretch such as initial aspect ratio, final aspect ratio, and strike time – which affects the initial extension rate – have been shown to dramatically impact resulting measurements of λ_E and η_E in self-assembled WLM fluids.[20,21] Prior work by Miller *et al.*[20] demonstrated that λ_E and η_E of the WLM solutions decreased with in-

Table 2 Summary of surfactant and polymer WLM structural, shear rheology, and extensional rheology parameters; data was digitized from the appropriate reference when necessary. Compositions are given as %wt or as a ratio of surfactant to salt (in mM). In 'Method,' D corresponds to DoS, C corresponds to CaBER, and F corresponds to FiSER; for reviews on WLMs in these and other extensional flows, see refs. 85–87. For morphology, micelles are categorized as either linear (L) or branched (B); CTAB/NaSal WLMs examined by Bhardwaj *et al.*[43] and EHAC/NH_4Cl WLMs examined by Yesilata *et al.*[44] are inferred as branched based on reported rheology and prior work.[40,88] Additional experiments on similar systems reported by Sachsenheimer et al.,[40] Miller et al.,[20] Wu et al.,[31] Haward and McKinley[89], Chellamuthu and Rothstein,[62] and Wu and Mohammadigoushki[90] are listed in 'See ref.'

Ref.	Method	System	Comp. [%wt or mM surf./salt]	Morph.	R [Å]	L_c [μm]	η_0 [Pa·s]	G_0 [Pa]	λ_s [s]	λ_E [s]	Tr_{max}	See ref.
This work	D	P234/NaF D_2O	4%/ 0.9 M	L	64[45]	0.4[a] 0.8	1.5 25	1.6 2.8	1.2 11.7	0.030 8.4 (I), 18.6 (III)	11 270	-
Omidvar et al.[36]	C	CTAT	0.7 - 0.9% 3 - 5%	L	-	0.05 - 0.06 6.0 - 4.4	-	-	- 60.2 - 18.8	0.039 - 0.022 2.02 - 1.1	$2{\cdot}10^5$ - $2{\cdot}10^4$ 4.5 - 3.1	-
Kim et al.[21]	C	CPyCl/NaSal 100 mM NaCl	100/50	L	-	0.61	17	24	0.88	0.81	50	-
Bhardwaj et al.[43]	C, F	CPyCl/NaSal 100 mM NaCl	50/25 100/50 150/75 200/100	L	-	0.79 1.1 1.3 1.1	1 11 30 69	4.2 27 60 104	0.55 1.2 1.4 1.6	0.12 0.52 1.3 1.8	610[c] 45[c], 150 - 500[f] 30[c], 94 - 950[f] 13[c], 60 - 410[f]	40, 20, 89
Bhardwaj et al.[43]	C, F	CTAB/NaSal	10/10 17.5/17.5 25/25 50/50 75/75 100/100 150/150	B[40]	22[91]	6.8 5.2 2.4[b] 1.5[b] 0.86[b] 0.66[b] 0.68[b]	5.0 41 68 62 55 39 38	0.28 1.2 2.5 10.9 26.2 48.8 94.8	17 35 33 5.7 2.2 0.80 0.44	2.1 8.6 14 6.1 2.0 1.0 -	1400[c] 230[c] 130[c] 160[c] 100[c] 90[c] 4[c]	-
Yesilata et al.[44]	C	EHAC/NH_4Cl	54/572 54/718 54/864	B[88]	-	2.6 2.5 2.1	238 126 59	8.4 11.6 11.8	28.4 10.9 5	9.03 3.63 1.65	50 37 84	-
Omidvar et al.[32]	C, D	CPyCl/NaSal	100/53 100/70 100/80 100/85.5	L B B B	-	0.22[b] 1.3[b] 0.5[b] 0.24[b]	2.8 53.2 10.0 2.83	12 36 40 38	3.96 14.6 2.4 0.59	0.23[c], 0.24[d] 1.2[c], 4.2[d] 0.39[c], 0.62[d] 0.19[c], 0.35[d]	3980[c], 11900[d] 45[c], 400[d] 120[c], 400[d] 200[c], 2340[d]	31, 89
Omidvar et al.[32]	C, D	OTAB/NaOA, 3% surf. total	0.75 / 2.25% 0.825 / 2.175% 0.9 / 2.1% 1.05 / 1.95% 1.2 /1.8% 1.3 /1.7% 1.5 / 1.5% 1.8 / 1.2% 2.1 / 0.9%	L	-	-	29 220 600 320 61 21 2.4 0.4 0.07	- 18 17 18 - 19 13 6.7 -	6.9 38 60 23 3.1 1.4 0.18 0.05 -	3.4[c], 4.2[d] 13[c], 16[d] 11[c], 17[d] 0.9[c], 1.8[d] 0.3[c], 0.4[d] 0.2[c], 0.3[d] 0.07[c], 0.10[d] 0.03[c], 0.06[d] 0.01[c], 0.03[d]	320[c], 1530[d] 40[c], 160[d] 9[c], 36[d] 6[c], 44[d] 19[c], 41[d] 13[c], 77[d] 90[c], 220[d] 510[c], 1730[d] 650[c], 3210[d]	31, 62
Wu & Mohammadigoushki[37]	C, D	CPyCl/NaSal	25/18.5 25/18.8 25/20.5	L L B onset	-	-	5.9 15.5 54.9	0.4 0.8 2.2	16.5 20.5 24.5	2.5[c], 11.3[d] 4.9[c], 3.3[d] 5.7[c], 20.1[d]	1600[c] 770[c] 230[c]	90
Calabrese & Wagner[84]	C	CTAT/SDBS (1.5%) +NaTos	0.01% 0.10%	L B	21.3 20.4	0.8 1.3	34 2.6	7.4 7.2	5.9 0.39	1.8 0.46	40 120	-
Zhao, Shen, & Haward[92]	C	CTAB/SHNC	60/19	B	-	-	130	10	50	45.4	≈200	-

[a]estimated despite absence of G''_{min} [b]incomplete frequency range [c]performed with CaBER [d]performed with DoS [f]performed with FiSER

creasing initial extension rate and increasing final aspect ratio. Moreover, the range of Tr_{max} reported in the study by Kim *et al.* [21] spanned up to one order of magnitude as a result of varying the final aspect ratio from 0.78 to 1.05 (Table 2). Differences in CaBER instrument parameters can also preclude direct comparison of the same system across different studies. For example, Kim *et al.* [21] and Bhardwaj *et al.* [43] both conducted CaBER measurements of 100/50 CPyCl/NaSal WLMs but report different λ_E and Tr_{max} values (Table 2). While the differences in extracted extensional parameters could be attributed to differences in sample preparation, the final CaBER aspect ratios are not always explicitly reported, thus complicating the deconvolution of instrument and sample effects in understanding differences between extracted extensional parameters.

FiSER measurements have also been used for WLM extensional rheology; however, because FiSER is conducted differently than CaBER, the two methods can give rise to very different results in extensional measurements of WLM solutions. To induce extensional flow, FiSER employs a constant extension rate by applying an exponential displacement profile. The difficulty in applying this displacement profile has limited the typical constant extension rates imposed during FiSER to between ~0.1 and ~10 s^{-1} (see Table 2; ref. 43). Similar to CaBER, the FiSER extension rate also impacts the value of η_E in WLM systems, as shown by Bhardwaj *et al.* [43] who reported a decrease in Tr_{max} with increasing extension rate for CPyCl/NaSal WLMs (Table 2). In contrast to FiSER, the extension rate varies continuously throughout a given measurement in capillary thinning based methods (CaBER and DoS); in the DoS measurements herein (Figure S9) and in CaBER measurements by Kim *et al.* [21], extension rates spanned $O(10^{-1})$ to $O(10^{1})$ in a single experiment. Additionally, in direct comparisons between CaBER and FiSER measurements of CPyCl/NaSal WLMs, [43] the extensional viscosities measured in FiSER were consistently higher than those from CaBER, likely due to the rapid step-stretch in CaBER (Table 2).

Direct comparisons between CaBER and DoS suggest that DoS should be used preferentially for measuring self-assembled fluids because DoS is less disruptive to fluid microstructure with the low droplet dispensing rate and lack of step-stretch. As aforementioned, Omidvar *et al.* [32] found that Tr (and thus η_E), extensional relaxation time λ_E, and filament lifetime were always greater in DoS than in CaBER measurements (Table 2). The authors attributed these differences to flow-induced micellar scission during the CaBER pre-stretch; this hypothesis was supported by measurements on WLMs outside of the fast-breaking regime, which showed only small differences in the extracted DoS versus CaBER parameters. [32] To expand on these findings and those of Sachsenheimer *et al.* [40], Tr_{max} from CaBER and DoS for all linear fast-breaking WLMs reported in Table 2 is shown as a function of relaxation time ratio, λ_E/λ_s, in Figure 7 below. Note that WLMs that do not exhibit a true plateau modulus or that exhibit deviations from semi-circular behavior in the Cole-Cole plot of the reported LVE data are not included; in most of these cases, $\lambda_E/\lambda_s < 0.2$. However, despite guidelines defined by Sachsenheimer *et al.* [40] where $\lambda_E/\lambda_s \approx 1$ corresponds to fast-breaking micelles, here LVE rheology is used as a more accurate selection criterion, as many WLMs with $\lambda_E/\lambda_s < 0.2$ exhibit fast-breaking behavior.

For linear fast-breaking WLMs measured via CaBER, the maximum Trouton ratio is limited to $Tr_{max} \approx 100$ (Figure 7, blue symbols). This apparent limit in Tr_{max} is consistent with the hypothesis of flow-induced micellar scission during the CaBER pre-stretch, [32] which could preclude higher Tr_{max} from being achieved. Additionally, Tr_{max} shows no apparent correlation with increasing λ_E/λ_s in CaBER, despite the increasing relative prominence of the extensional relaxation mode; CaBER data is subdivided into distinct symbols based on reference to confirm that even when sample type and instrument operating parameters are held constant, no trends are observed between Tr_{max} and λ_E/λ_s. Note that the CTAB/NaSal WLMs used by Bhardwaj *et al.* [43] are thought to be branched based on prior literature [40] and are thus not included in Figure 7; however, if these data are included, the same trend in the CaBER data is observed but a slightly higher Tr_{max} is achieved (see SI.11).

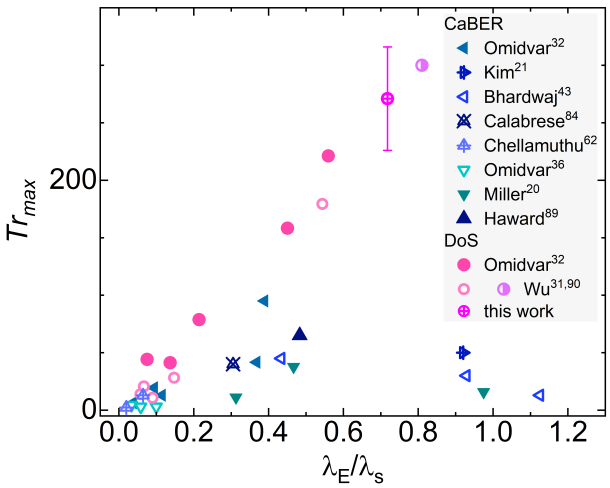

Fig. 7 Tr_{max} for fast-breaking WLMs as a function of relaxation time ratio, λ_E/λ_s, measured in CaBER (blue symbols, refs. 20,21,32,36,43, 62,84,89) vs. DoS (pink •, refs. 31,32,90 and this work [39 °C]). Error bars (when reported) are the 95% confidence interval from multiple trials. WLMs measured via DoS show a clear increase in Tr_{max} with increasing λ_E/λ_s; corresponding CaBER trials appear randomly distributed, likely due to breakage during the initial step strain. CaBER trials coded by sample and reference show that even within the same system or operating parameters, no trend in Tr_{max} with increasing λ_E/λ_s is observed.

In contrast, larger Tr_{max} are observed in DoS measurements, and Tr_{max} increases monotonically with increasing λ_E/λ_s. This finding is perhaps unsurprising given that $Tr_{max}$is directly related to WLM finite extensibility, where $Tr_{max} \approx 2L^2$ in the limit of high Wi and for systems where $\eta_E > \eta_s$. Notably, these DoS data appear to collapse onto a single curve despite differences in experimental set-up. [31,32] When equivalent CaBER vs. DoS data by Omidvar *et al.* [32] are compared, Tr_{max} from DoS shows a statistically significant increase with λ_E/λ_s whereas corresponding Tr_{max} from CaBER shows no statistically significant changes with λ_E/λ_s (see SI.11). These findings suggest that not only should care be taken when comparing DoS and CaBER measurements – as CaBER values will likely underestimate values that would be obtained via DoS – but also that CaBER does not consistently underestimate DoS results, even for WLMs that are deemed fast-

breaking based on LVE rheology. Instead, the difference in parameters extracted between the two methods appears to increase with increasing λ_E/λ_s, as λ_E/λ_s approaches the value of unity set forth by Sachsenheimer *et al.* [40] for 'fast-breaking' WLMs. As such, important trends in the extensional flow behavior with respect to WLM shear rheological parameters may be missed or misrepresented by CaBER measurements.

5 Conclusions

We developed an environmental chamber with heaters for the nozzle, substrate, and enclosure to enable temperature-controlled dripping-onto-substrate (TC-DoS) measurements for the first time. At ambient temperature, spherical P234 micelle solutions exhibit inertiocapillary thinning similar to that of pure D_2O, but with longer breakup times due to reduced surface tension. With increasing temperature above the sphere-to-rod transition, micelle growth increases the shear viscosity substantially and causes thinning at early times to evolve towards viscocapillary behavior, increasing overall breakup times. As micelles elongate further from rods to wormlike micelles (WLMs) at higher temperatures, the extensional relaxation time dramatically increases, and the Trouton ratio plateaus, reaching $Tr_{max} \sim O(10^2)$ at high Hencky strains. These TC-DoS measurements of polymer WLMs illuminate the similarities in WLM extensional flow behavior across polymer and surfactant WLMs despite vast differences in WLM cross-sectional radius or amphiphile molecular weight.

The exceptionally slow dynamics of P234 WLMs enabled the identification of distinct elastic thinning regimes that correspond to elastocapillary thinning, formation of beads-on-a-string (BOAS) instabilities, and BOAS thinning. In contrast to PEO solutions in prior studies that formed up to four generations of beads, the BOAS instabilities observed in nonionic polymer WLMs herein largely consisted of a single generation of lemon-shaped beads, with some trials exhibiting a second generation of much smaller beads. The less developed BOAS instability in P234 WLMs is attributed to the relatively high zero-shear viscosity that dampens elastic effects.

Comparing the extensional behavior of polymer and surfactant WLMs across prior literature highlights that differences between extensional rheology methods (CaBER, FiSER, DoS) limit the scope of sound comparisons to measurements within a single study or to different studies using the same technique and instrument parameters. Comparing extensional rheology parameters such as maximum Tr and relaxation time ratio (λ_E/λ_s) acquired using DoS to those acquired using CaBER reveals that the step-stretch in CaBER can mask important trends in flow behavior and cause extensional rheology parameters to be under-predicted, the degree to which depends on λ_E/λ_s. Until now, one major advantage of CaBER over DoS or FiSER was the ability to control sample temperature, albeit not very precisely given that the sample chamber is not well-sealed. However, given these new advancements in TC-DoS, DoS rheometry appears to be the most promising method for measuring fluids with sensitive microstructures due to the minimal pre-deformation involved, relative ease in creating the liquid bridge, and the ability to measure fluids with a wide range of viscosities.

Conflicts of interest

There are no conflicts to declare.

Acknowledgements

The authors thank KT Lauser for the edge detection MATLAB code used to generate radius evolution curves and BP Robertson for the MATLAB code used to determine bead size and velocities. This material is based upon work supported by the National Science Foundation Graduate Research Fellowship under Grant No. CON-75851, project 00074041. Any opinions, findings, and conclusions or recommendations expressed in this material are those of the author(s) and do not necessarily reflect the views of the National Science Foundation. The authors thank the Anton Paar VIP program for the shear rheometer used in this work.

Notes and references

1 I. Makhnenko, E. R. Alonzi, S. A. Fredericks, C. M. Colby and C. S. Dutcher, *J. Aerosol Sci.*, 2021, **157**, 105805.
2 R. P. Mun, B. W. Young and D. V. Boger, *J. Non-Newton. Fluid Mech.*, 1999, **83**, 163–178.
3 E. Tekin, P. J. Smith and U. S. Schubert, *Soft Matter*, 2008, **4**, 703–713.
4 P. Calvert, *Chem. Mater.*, 2001, **13**, 3299–3305.
5 Y. Christanti and L. M. Walker, *J. Non-Newton. Fluid Mech.*, 2001, **100**, 9–26.
6 M. S. Owens, M. Vinjamur, L. E. Scriven and C. W. Macosko, *Ind. Eng. Chem. Res.*, 2011, **50**, 3212–3219.
7 M. S. Owens, M. Vinjamur, L. Scriven and C. Macosko, *J. Non-Newton. Fluid Mech.*, 2011, **166**, 1123–1128.
8 S. Kumar, *Annu. Rev. Fluid Mech.*, 2015, **47**, 67–94.
9 W. C. Hoffmann, B. K. Fritz and D. E. Martin, *Agric. Eng. Int.: CIGR J.*, 2011, **13**,.
10 U. Sen, C. Datt, T. Segers, H. Wijshoff, J. H. Snoeijer, M. Versluis and D. Lohse, *J. Fluid Mech.*, 2021, **929**, A25.
11 D. Xu, V. Sanchez-Romaguera, S. Barbosa, W. Travis, J. d. Wit, P. Swan and S. George Yeates, *J. Mater. Chem.*, 2007, **17**, 4902–4907.
12 C. McIlroy, O. G. Harlen and N. F. Morrison, *J. Non-Newton. Fluid Mech.*, 2013, **201**, 17–28.
13 A. Gaillard, R. Sijs and D. Bonn, *What determines the drop size in sprays of polymer solutions?*, 2021.
14 G. H. McKinley, *Rheol. Rev.*, 2005, 1–48.
15 L. E. Rodd, T. P. Scott, J. J. Cooper-White and G. H. McKinley, *Appl. Rheol*, 2005, **15**, 12–27.
16 J. Dinic, Y. Zhang, L. N. Jimenez and V. Sharma, *ACS Macro Lett.*, 2015, **4**, 804–808.
17 L. Campo-Deaño and C. Clasen, *J. Non-Newton. Fluid Mech.*, 2010, **165**, 1688–1699.
18 D. C. Vadillo, W. Mathues and C. Clasen, *Rheol. Acta*, 2012, **51**, 755–769.
19 V. Sharma, S. J. Haward, J. Serdy, B. Keshavarz, A. Soderlund, P. Threlfall-Holmes and G. H. McKinley, *Soft Matter*, 2015, **11**, 3251–3270.

20 E. Miller, C. Clasen and J. P. Rothstein, *Rheol. Acta.*, 2009, **48**, 625–639.

21 N. J. Kim, C. J. Pipe, K. H. Ahn, S. J. Lee and G. H. McKinley, *Korea Aust. Rheol. J.*, 2010, **22**, 11.

22 J. Du, H. Ohtani, C. E. Owens, L. Zhang, K. Ellwood and G. H. McKinley, *J. Non-Newton. Fluid Mech.*, 2021, **291**, 104496.

23 B. P. Robertson and M. A. Calabrese, *Sci. Rep.*, 2021, **12**, 4697.

24 K. T. Lauser, A. L. Rueter and M. A. Calabrese, *Soft Matter*, 2021, **17**, 9624–9635.

25 J. Dinic and V. Sharma, *Macromolecules*, 2020, **53**, 3234–3437.

26 J. Dinic, M. Biagioli and V. Sharma, *J. Polym. Sci. B Polym. Phys.*, 2017, **55**, 1692–1704.

27 J. Dinic, L. N. Jimenez and V. Sharma, *Lab Chip*, 2017, **17**, 460–473.

28 J. Merchiers, C. D. V. Martínez Narváez, C. Slykas, N. K. Reddy and V. Sharma, *Macromolecules*, 2021, **54**, 11061–11073.

29 S. Sur, M. Chellamuthu and J. Rothstein, *Rheol. Acta.*, 2019, **58**, 557–572.

30 J. Van Aeken, L. Passaro and C. Clasen, *Rheol. Acta*, 2022, **61**, 191–206.

31 S. Wu and H. Mohammadigoushki, *Phys. Rev. Fluids*, 2020, **5**, 053303.

32 R. Omidvar, S. Wu and H. Mohammadigoushki, *J. Rheol.*, 2019, **63**, 33–44.

33 E. Ewaldz, J. Randrup and B. Brettmann, *ACS Polym. Au*, 2021.

34 M. Xu, X. Li, A. Riseman and J. M. Frostad, *Phys. Fluids*, 2021, **33**, 032107.

35 Y. Zhang and S. J. Muller, *Phys. Rev. Fluids*, 2018, **3**, 043301.

36 R. Omidvar, A. Dalili, A. Mir and H. Mohammadigoushki, *J. Non-Newton. Fluid Mech.*, 2018, **252**, 48–56.

37 S. Wu and H. Mohammadigoushki, *J. Rheol.*, 2018, **62**, 1061–1069.

38 M. A. Calabrese and N. J. Wagner, *ACS Macro Lett.*, 2018, **7**, 614–618.

39 M. E. Helgeson, M. D. Reichert, Y. T. Hu and N. J. Wagner, *Soft Matter*, 2009, **5**, 3858–3869.

40 D. Sachsenheimer, C. Oelschlaeger, S. Müller, J. Küstner, S. Bindgen and N. Willenbacher, *J. Rheol.*, 2014, **58**, 2017–2042.

41 R. Zana and E. W. Kaler, *Giant micelles: Properties and Applications*, CRC press, 2007, vol. 140.

42 M. Fardin, T. Ober, V. Grenard, T. Divoux, S. Manneville, G. McKinley and S. Lerouge, *Soft Matter*, 2012, **8**, 10072–10089.

43 A. Bhardwaj, E. Miller and J. P. Rothstein, *J. Rheol.*, 2007, **51**, 693–719.

44 B. Yesilata, C. Clasen and G. H. McKinley, *J. Non-Newton. Fluid Mech.*, 2006, **133**, 73–90.

45 P. J. McCauley, S. Kumar and M. A. Calabrese, *Langmuir*, 2021, **37**, 11676–11687.

46 S. Sur and J. Rothstein, *J. Rheol.*, 2018, **62**, 1245–1259.

47 J. Schindelin, I. Arganda-Carreras, E. Frise, V. Kaynig, M. Longair, T. Pietzsch, S. Preibisch, C. Rueden, S. Saalfeld, B. Schmid, J.-Y. Tinevez, D. J. White, V. Hartenstein, K. Eliceiri, P. Tomancak and A. Cardona, *Nat. Methods*, 2012, **9**, 676–682.

48 A. Daerr and A. Mogne, *J. Open Res. Softw.*, 2016, **4**, p.e3.

49 C. Wohlfarth and M. D. Lechner, *Surface Tension of Pure Liquids and Binary Liquid Mixtures*, Springer-Verlag Berlin Heidelberg, 2016, vol. 28.

50 J. R. Castrejón-Pita, A. A. Castrejón-Pita, E. J. Hinch, J. R. Lister and I. M. Hutchings, *Phys. Rev. E*, 2012, **86**, 015301.

51 R. F. Day, E. J. Hinch and J. R. Lister, *Phys. Rev. Lett.*, 1998, **80**, 704–707.

52 Y. Amarouchene, D. Bonn, J. Meunier and H. Kellay, *Phys. Rev. Lett.*, 2001, **86**, 3558–3561.

53 C. Wagner, Y. Amarouchene, D. Bonn and J. Eggers, *Phys. Rev. Lett.*, 2005, **95**, 164504.

54 J. Dinic and V. Sharma, *Phys. Fluids*, 2019, **31**, 021211.

55 A. Deblais, M. Herrada, I. Hauner, K. Velikov, T. van Roon, H. Kellay, J. Eggers and D. Bonn, *Phys. Rev. Lett.*, 2018, **121**, 254501.

56 D. H. Peregrine, G. Shoker and A. Symon, *J. Fluid Mech.*, 1990, **212**, 25.

57 C. D. V. Martínez Narváez, J. Dinic, X. Lu, C. Wang, R. Rock, H. Sun and V. Sharma, *Macromolecules*, 2021, **54**, 6372––6388.

58 D. T. Papageorgiou, *Phys. Fluids*, 1995, **7**, 1529–1544.

59 G. H. McKinley and A. Tripathi, *J. Rheol.*, 2000, **44**, 653–670.

60 S. L. Anna and G. H. McKinley, *J. Rheol.*, 2000, **45**, 115–138.

61 L. N. Jimenez, C. D. V. Martínez Narváez and V. Sharma, *Phys. Fluids*, 2020, **32**, 012113.

62 M. Chellamuthu and J. P. Rothstein, *J. Rheol.*, 2008, **52**, 865–884.

63 A. Bhardwaj, D. Richter, M. Chellamuthu and J. P. Rothstein, *Rheol. Acta*, 2007, **46**, 861–875.

64 R. Granek and M. E. Cates, *J. Chem. Phys*, 1992, **96**, 4758.

65 V. Entov and E. Hinch, *J. Non-Newton. Fluid Mech.*, 1997, **72**, 31–53.

66 J. Li and M. A. Fontelos, *Phys. Fluids*, 2003, **15**, 922–937.

67 C. Clasen, J. Eggers, M. A. Fontelos, J. Li and G. H. McKINLEY, *J. Fluid Mech.*, 2006, **556**, 283.

68 A. M. Ardekani, V. Sharma and G. H. McKinley, *J. Fluid Mech.*, 2010, **665**, 46–56.

69 M. S. N. Oliveira and G. H. McKinley, *Phys. Fluids*, 2005, **17**, 071704.

70 M. S. N. Oliveira, R. Yeh and G. H. McKinley, *J. Non-Newton. Fluid Mech.*, 2006, **137**, 137–148.

71 R. Sattler, C. Wagner and J. Eggers, *Phys. Rev. Lett.*, 2008, **100**, 164502.

72 J. Dinic and V. Sharma, *Proc. Natl. Acad. Sci.*, 2019, **116**, 8766–8774.

73 R. K. Gupta, D. A. Nguyen and T. Sridhar, *Phys. Fluids*, 2000, **12**, 1296–1318.

74 R. P. Mun, J. A. Byars and D. V. Boger, *J. Non-Newton. Fluid*

Mech., 1998, **74**, 285–297.
75 R. Sattler, S. Gier, J. Eggers and C. Wagner, *Phys. Fluids*, 2012, **24**, 023101.
76 H.-C. Chang, E. A. Demekhin and E. Kalaidin, *Phys. Fluids*, 1999, **11**, 1717–1737.
77 C. L. Lee, T. S. Chan, A. Carlson and K. Dalnoki-Veress, *Soft Matter*, 2022, **18**, 1364–1370.
78 J. Eggers, *Phys. Fluids*, 2014, **26**, 033106.
79 A. Deblais, K. Velikov and D. Bonn, *Phys. Rev. Lett.*, 2018, **120**, 194501.
80 P. P. Bhat, S. Appathurai, M. T. Harris, M. Pasquali, G. H. McKinley and O. A. Basaran, *Nat. Phys.*, 2010, **6**, 625–631.
81 M. C. Sostarecz and A. Belmonte, *Phys. Fluids*, 2004, **16**, L67–L70.
82 J. P. Rothstein, *J. Rheol.*, 2003, **47**, 1227–1247.
83 L. B. Smolka and A. Belmonte, *J. Non-Newton. Fluid Mech.*, 2003, **115**, 1–25.
84 M. A. Calabrese, *Developing structure-property relationships in branched wormlike micelles via advanced rheological and neutron scattering techniques*, University of Delaware, 2017.
85 J. P. Rothstein and H. Mohammadigoushki, *J. Non-Newton. Fluid Mech.*, 2020, **285**, 104382.
86 J. P. Rothstein, *Rheol. Rev*, 2008, **1**, 1–46.
87 Y. Zhao, P. Cheung and A. Q. Shen, *Adv. Colloid Interface Sci.*, 2014, **211**, 34–46.
88 S. R. Raghavan, H. Edlund and E. W. Kaler, *Langmuir*, 2002, **18**, 1056–1064.
89 S. J. Haward and G. H. McKinley, *Phys. Rev. E*, 2012, **85**, 031502.
90 S. Wu and H. Mohammadigoushki, *Soft Matter*, 2021, **17**, 4395–4406.
91 C. N. Lam, C. Do, Y. Wang, G.-R. Huang and W.-R. Chen, *Phys. Chem. Chem. Phys.*, 2019, **21**, 18346–18351.
92 Y. Zhao, A. Q. Shen and S. J. Haward, *Soft Matter*, 2016, **12**, 8666–8681.